

Flow noise estimation models for axial flow past towed sonar arrays

Rakesh Sekharipuram Sekar

Department of Mechanical Engineering,
Indian Institute of Technology Palakkad,
Palakkad, Kerala, 678003, India
Email: 132203001@smail.iitpkd.ac.in

Senthil Rajan S

Naval Physical Oceanographic Laboratory,
Ernakulam, Kerala, 682021, India
Email: senthilrajan.npol@gov.in

Anoop Akkoorath Mana*

Department of Mechanical Engineering,
Indian Institute of Technology Palakkad,
Palakkad, Kerala, 678003, India
Email: akkoorath@iitpkd.ac.in

ABSTRACT

Towed sonar arrays house a series of pressure sensors inside a fluid-filled elastic tube. Towing of the sonar array in water generates a turbulent boundary layer on the exterior surface of the elastic tube. The pressure fluctuations in the turbulent boundary layer along with other ambient pressure fluctuations, excites the elastic tube and further generates pressure disturbances in the interior fluid. In this work, a new semi-empirical model of the turbulent pressure spectrum is presented. The new model predictions show a closer agreement with the available experimental results at all tow speeds. A three-dimensional vibroacoustic model of the fluid-filled elastic tube is also presented in this work. The vibroacoustic model is fully coupled and considers both breathing mode and first order variations in the elastic tube and the acoustic field variables. Further, the turbulent pressure spectrum semi-empirical model and the three-dimensional vibroacoustic model are used to compute

*Address all correspondence for other issues to this author.

the on-axis sound pressure level due to the external turbulent pressure excitation at different elastic tube diameters and tow speeds. At low frequencies, increasing tube diameter has little effect on flow noise, while at higher frequencies, flow noise decreases with larger diameters. Increasing tow speed raises flow noise across all frequencies.

INTRODUCTION

Towed sonar arrays contain a series of pressure sensors enclosed within a fluid-filled elastic tube. As the sonar array is towed through the water, a thick layer of turbulent flow is generated over the exterior surface of the tube. The pressure fluctuations in this turbulent boundary layer (TBL), along with other ambient sea pressure variations, excite the elastic tube and subsequently produce acoustic pressure disturbances within the interior fluid. The hydrophones placed in the interior fluid picks these acoustic signals. The signals associated with the turbulent pressure fluctuations are called flow noise. Currently, the flow noise is measured either by towing the sonar array in open water using a dinghy or by allowing the hydrophone to free fall in water [1]. In the first case, noise from the boat and vibrations of the towline connections pollute the measured acoustic signals [2]; whereas in the second case, the useful measurements can be made only at the terminal velocity of the hydrophone. This work aims at developing a fully-coupled vibroacoustic model for predicting the flow noise in towed sonar arrays which is useful over wide range of towing speeds and tube diameters.

A widely used model for predicting the turbulent pressure spectrum is that developed by Corcos [3] for the flow over a flat plate. In this model, the turbulent pressure is varying exponentially with respect to both the axes of the flat plate. Although this model is widely used in engineering applications, it has a major shortcoming that it is overestimating the pressure level at low wavenumbers. Chase [4] presented a simpler turbulent pressure spectrum model for the flow over a flat plate. The model is based on experimental observations and uses direct dependence on the flow and dimensional parameters. Frendi and Zhang [5] analysed the Corcos [3] model and proposed a turbulent model for the flow over a flat plate based on large eddy simulation (LES) and direct numerical simulation (DNS) computational results. Frendi's model involves the use of an

auto spectrum which was derived by Goody [6]. The Frendi model predictions are found to match well with an earlier experimental result on flow over a flat plate. Some of the observations of the Chase and Frendi models are relevant to the present work and are discussed in section 1. Francis *et al.* [7] used LES and Reynolds averaged Navier Stokes (RANS) computational method to study the wavenumber frequency spectrum of the turbulent pressure field over a flat plate. This work presents an exhaustive discussion on similar problems in the literature.

Chase [4] developed a model for computing the turbulent pressure spectrum for an axial flow past a cylinder by modifying his earlier flat plate model. While modifying, Chase considered the radius of the cylinder as one of the parameters instead of the length of the flat plate. Chase derived azimuthal harmonic spectral density by integrating the turbulent pressure spectrum of the flat plate in the cross-flow direction. The details of this model are presented in section 1.1.

Carpenter and Kewley [8] conducted experiments for finding the flow noise inside a fluid-filled elastic tube while towed behind a ship and compared the results with that predicted by Chase [4]. The authors also proposed a tube transfer function for computing the flow noise inside the tube. Knight [9] performed similar analytical simulations as in [8] but with different types of hydrophones and compared the flow noise with that for an ideal hydrophone. The ideal hydrophone was assumed to have unit acoustic response and zero convective response. Knight also used an approximate tube transfer function to find the noise inside the fluid-filled elastic tube.

Unnikrishnan *et al.* [2] performed experiments to measure the turbulent pressure field outside the elastic tube by towing the sonar array in a quiet lake at different speeds. The work presents a comparison of the experimental results with the available semi-empirical model predictions. It was found that the semi-empirical model estimations match with the measurements only at high tow speeds. Karthik *et al.* [10] studied the turbulent pressure spectrum over a cylinder with the help of an LES computational model. The model predictions match well with the experimental results of Unnikrishnan *et al.* [2]. Karthik *et al.* also presented a non-dimensional turbulent flow noise spectrum for easy estimation of the spectrum at different tow speeds and tube diameters.

Both Carpenter and Kewley [8] and Knight [9] estimated the flow noise inside a fluid-filled elastic tube with the help of the Chase model for the turbulent pressure spectrum and an approximate

51 tube transfer function. Jineesh and Ebenezer [11] developed a better axisymmetric model of the
52 fluid-filled elastic tube and used it to estimate the flow noise inside the tube. It was found that the
53 earlier approximate transfer function model overestimated the flow noise inside the tube.

54 This paper develops a new semi-empirical model of the turbulent pressure spectrum for axial
55 flow past a solid cylinder. It also presents a fully coupled three-dimensional vibroacoustic model
56 of a fluid-filled elastic tube. Furthermore, these two models are used to compute the on-axis
57 sound pressure level resulting from an external turbulent pressure excitation on the elastic tube.
58 This paper is organized as follows: Section 1 discusses two existing semi-empirical models for
59 estimating turbulent pressure spectrum for axial flow past a solid cylinder. Section 2 discusses the
60 development of a new semi-empirical model for the turbulent pressure spectrum, which provides
61 improved predictions compared to existing models. Section 3 discusses the development of a
62 three-dimensional vibroacoustic model for estimating the on-axis flow noise inside a fluid-filled
63 elastic tube. Further, Section 4 presents the results on interior acoustic pressure spectrum and
64 on-axis flow noise inside a fluid-filled elastic tube and are compared with the available results in
65 the literature.

1 REVIEW OF SEMI-EMPIRICAL MODELS OF TURBULENT PRESSURE SPECTRUM

66 One of the objective of this study is to predict the flow noise resulting from turbulent boundary
67 layer excitation. To achieve this, a semi-empirical model that can estimate the turbulent pressure
68 exerted by fluid flow on a cylindrical tube, is required. Two existing semi-empirical models for
69 turbulent pressure fluctuation are discussed in this section. Further, flow noise at the outer surface
70 of the tube is estimated using these models, showing its variation in comparison to available
71 experimental results [2].

72 1.1 Chase model

73 Chase [4] proposed a semi-empirical model for predicting the frequency-wavenumber spec-
74 trum of turbulent pressure field over a solid cylinder and is given by

$$\hat{p}_0(k_z, \omega) = C \rho^2 \nu_*^3 R^2 \left[(k_z R)^2 + \frac{1}{12} \right] \times \left[\frac{(\omega R - u_c k_z R)^2}{h^2 \nu_*^2} + (k_z R)^2 + b_1^{-2} \right]^{-2.5}. \quad (1)$$

75 The important parameters in the above equation are axial wavenumber k_z , frequency ω , density
76 of the fluid ρ , convective speed u_c ($= 0.68u$, where u is the tow speed), $C = 0.063$, $h = 3.7$,
77 $\nu_* = 0.04U$ and tube radius R [4, 8, 9, 12, 13].

78 1.2 Frendi model

79 Frendi's model for the turbulent pressure spectrum for a flat plate is given by [5]

$$\hat{R}(k_z, k_2, \omega) = C_1 R^* (\omega) e^{-\hat{\alpha} r_k}. \quad (2)$$

80 In the above equation, C_1 is given by

$$C_1 = \alpha^2 m \delta^2 \frac{1}{2\pi}, \quad (3)$$

81 where α can be computed using

$$\alpha = \frac{a_1}{\pi} \frac{1}{\sqrt{1 + a_2 \left(\frac{\omega \delta}{u_t} - 50 \right)^2}}. \quad (4)$$

82 In the above equation, $a_1 = 4.7$, $a_2 = 3 \times 10^{-5}$ [5], u_t is the friction velocity ($=0.04u$, a small fraction
83 of tow velocity u) and δ is the boundary layer thickness [14] given by

$$\delta = [48Re_a^{-1}Re_x^{(0.0226 \log Re_a + 0.2478)}]^{1/0.91}. \quad (5)$$

84 In the above equation, Re_a is the radius based Reynold's number ($\frac{\rho u R}{\mu}$) and Re_x is length based
85 Reynold's number ($\frac{\rho u x}{\mu}$), x is distance of a point on the cylinder from the leading edge and μ is
86 the dynamic viscosity of the fluid medium. The constant m in Eq. (3) is a scaling factor which is
87 approximately taken as $1/7.7$ [5].

88 $R^*(\omega)$ in Eq. (2) is the auto-spectrum given by [6]

$$R^*(\omega) = \frac{3\tau_w^2\omega^2(\frac{\delta}{u})^3}{[(\frac{\omega\delta}{u})^{0.75} + 0.5]^{3.7} + [1.1R_t^{-0.57}(\frac{\omega\delta}{u})]^7}. \quad (6)$$

89 In the above equation, τ_w is the shear stress at the wall, R_t is the ratio of time scale [6] given by

$$R_t = \left(\frac{u_t}{u}\right) \left(\frac{u_t\delta}{\nu}\right), \quad (7)$$

90 where ν is the kinematic viscosity.

91 $\hat{\alpha}$ in Eq. (2) is given by $\hat{\alpha} = \alpha\delta$ and r_k depends on the axial and crossflow wavenumbers and
92 is given by

$$|r_k|^2 = \left(k_z - \frac{\omega}{u_c}\right)^2 + (mk_2)^2. \quad (8)$$

93 In the above equation, k_2 denotes the cross flow wavenumber and u_c is the convective speed ($=$
94 $0.68u$, a large fraction of tow speed u). Eq. (2) can be modified for estimating turbulent pressure

95 spectrum for an axial flow past a solid cylinder as

$$\hat{p}_0(k_z, \omega) = \int_{-1/2R}^{1/2R} \hat{R}(k_z, k_2, \omega) dk_2. \quad (9)$$

96 The estimation of flow noise using the models discussed in this section and its comparison with
97 the findings of experiments are presented below.

98 1.3 Flow noise

99 Here, the estimation of flow noise, as measured by a series of hydrophones placed at the
100 outer surface of a solid cylinder, is discussed and compared with the experimental results [2]. The
101 flow noise associated with the turbulent pressure spectrum $p_0(k_z, \omega)$ as registered by an array of
102 hydrophones is [2]

$$Q(\omega) = \int_{-\infty}^{\infty} \hat{p}_0(k_z, \omega) H(k_z) dk_z. \quad (10)$$

103 In the above equation, $H(k_z)$ is the hydrophone response function. The hydrophone array is a set
104 of large number of similar elements with specific length arranged at a fixed distance apart. This
105 array acts as noise filter and its response is given by [2]

$$H(k_z) = \frac{\sin(k_z d N / 2)}{N \sin(k_z d / 2)} \frac{\sin(l k_z / 2)}{l k_z / 2}, \quad (11)$$

106 where N is the number of hydrophone elements in the array, d is the distance between two hy-
107 drophones and l is the length of individual hydrophones.

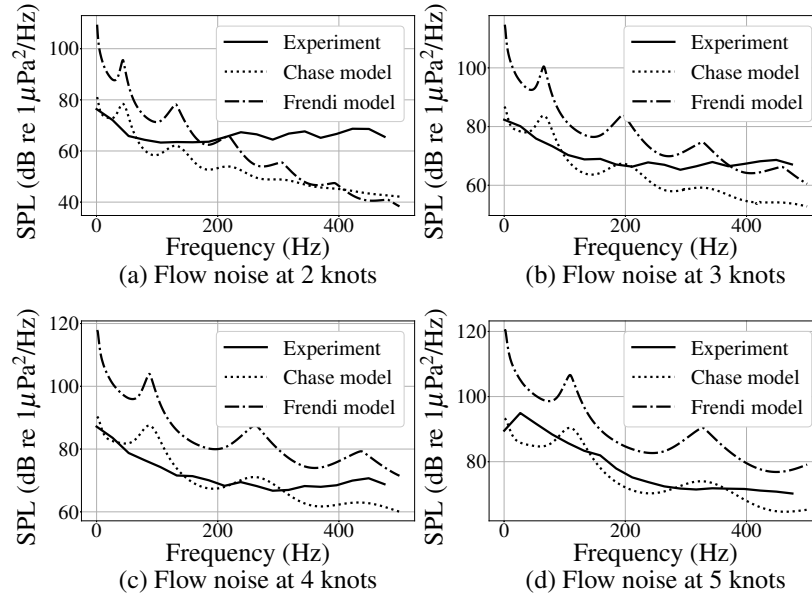


Fig. 1. Comparison of flow noise predicted by Chase [4] and Frendi [5] models with the experimental results [2] at different tow speeds.

108 The sound pressure level (SPL) associated with the flow noise $Q(\omega)$ is given by

$$SPL = 10 \log_{10} \left(\frac{Q(\omega)}{p_{ref}^2} \right), \quad (12)$$

109 where $p_{ref} = 1 \times 10^{-6}$ Pa is the reference acoustic pressure in water.

110 Figure 1 compares the flow noise estimated by the Chase [4] and Frendi [5] models with the
111 experimental results [2] at various tow speeds for a solid cylinder having a diameter of 0.01 m.
112 The sonar array consists of 66 hydrophones, each of length 8 mm, placed at the outer surface of
113 the cylinder with an interval of 16 mm. It is evident from Fig. 1 that the Frendi model consistently
114 overestimates the flow noise at almost all frequencies and tow speeds, whereas the Chase model
115 aligns well with experiments at high tow speeds. However, at low speeds, there is a significant dif-
116 ference between the Chase model and the experiment, especially at high frequencies. Regardless
117 of tow speed, both models predict a significant reduction in flow noise with frequency compared
118 to the experimental results. To address these differences, a new model of the turbulent pressure

119 spectrum is proposed in this work to better match the experimental data, particularly at low tow
120 speeds. The development of this new model is discussed in the following section.

2 A NEW SEMI-EMPIRICAL MODEL OF THE TURBULENT PRESSURE SPECTRUM

121 It is shown in the previous sections that the Chase and Frendi models show a significant
122 deviation from the experimental results [2] at low tow speeds and at high frequencies. In this
123 section, a new semi-empirical model of the turbulent pressure spectrum is developed that closely
124 aligns with the experimental results [2]. This new model is derived using the insights from both the
125 Chase and Frendi models and is referred to as the *hybrid model*.

126 2.1 The hybrid model

127 In the *hybrid model*, the pressure spectrum of the Chase model [4] (Section 1.1) is used in
128 conjunction with the exponential decay function present in the Frendi model [5] (Section 1.2).
129 Accordingly, the turbulent pressure spectrum is given by

$$\hat{p}(k_z, k_2, \omega) = C_3 \bar{P}(\omega) e^{-\hat{\alpha} r_k}. \quad (13)$$

130 In the above equation, the autospectrum $\bar{P}(\omega)$ is given by

$$\bar{P}(\omega) = \int_{-\infty}^{\infty} \hat{p}_0(\omega, k_z) dk_z, \quad (14)$$

131 where $\hat{p}_0(\omega, k_z)$ is the same as that used in the Chase model (Eq. (1)). In this new model, the
132 wavenumber dependency is included in the form of an exponential function $e^{-\hat{\alpha} r_k}$, where $\hat{\alpha} = \alpha \delta$
133 with

$$\alpha = \frac{a_1}{\pi} \frac{1}{\sqrt{1 + a_2 \left(\frac{\omega \delta}{u_t} - 50 \right)^2}}, \quad (15)$$

$$\delta = [48Re_a^{-1}Re_x^{(0.0226 \log Re_a + 0.2478)}]^{1/0.91} \quad (16)$$

134 and

$$|r_k|^2 = \left(k_z - \frac{\omega}{u_c}\right)^2 + (mk_2)^2. \quad (17)$$

135 In Eq. (15), a_1 and a_2 determine the behavior of the spectrum at low and high frequencies, respec-
 136 tively. It has been observed in Fig. 1 that the predictions of the Frendi model deviate more at higher
 137 frequency ranges. Therefore, the value of a_2 is decreased from 3×10^{-5} to 3×10^{-6} . Different
 138 values of a_1 and C_3 were tested to match the experimental results given in Fig. 1. A better match
 139 is found with the experimental data when $a_1 = 1$ and $C_3 = 1 \times 10^{-4}$. Furthermore, the turbulent
 140 pressure spectrum given in Eq. (13) is integrated over the cross-flow wavenumber k_2 from $-1/2R$
 141 to $1/2R$ to obtain the pressure spectrum $\hat{p}_0(k_z, \omega)$ for the axial flow past a solid cylinder [4]. Thus,

$$\hat{p}_0(k_z, \omega) = \int_{-1/2R}^{1/2R} \hat{p}(k_z, k_2, \omega) dk_2. \quad (18)$$

142 The hybrid model is used to compute the flow noise for axial flow past a solid cylinder. The
 143 results of the new model and their comparison with the existing models and Unnikrishnan's exper-
 144 imental results [2] are presented in the next subsection.

145 2.2 Flow noise

146 The flow noise can be computed using Eq. (10). Here, the turbulent pressure spectrum
 147 $\hat{p}_0(k_z, \omega)$ for the new hybrid model is given by Eq. (18) and the hydrophone response function
 148 $H(k_z)$ is given by Eq. (11). A comparison of flow noise measured in SPL (see Eq. (12)) computed
 149 using the new hybrid model, Chase model [4] and Unnikrishnan's experiment [2] are shown in
 150 Fig. 2. It can be seen that the predictions of the new hybrid model are consistent with the mea-

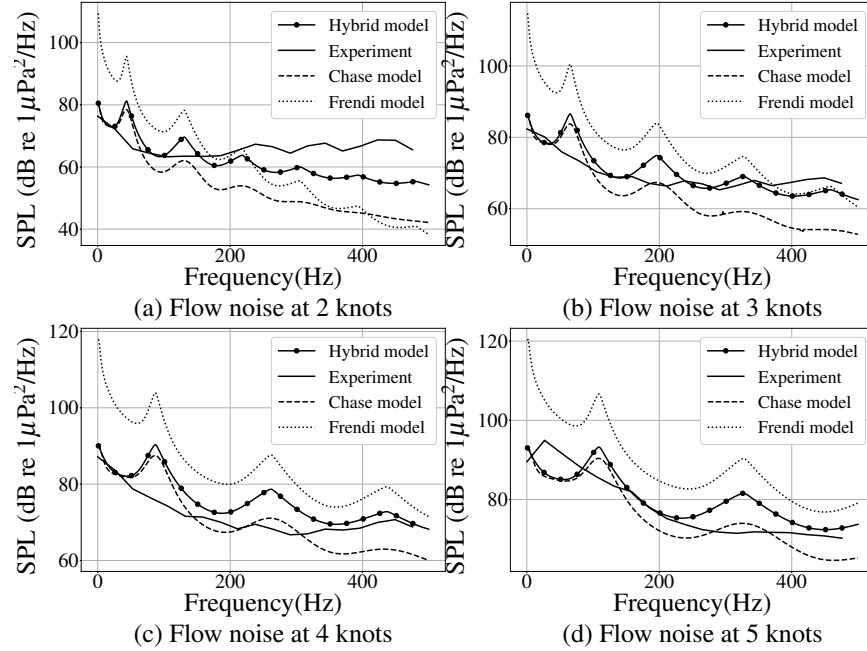


Fig. 2. A comparison of flow noise predicted by the hybrid model, the Chase model [4] and Frendi model [5] with that measured from experiments [2] at different tow speeds.

sured values [2] at all frequencies and towing speeds. Although the hybrid model underpredicts noise at high frequencies for the 2 knots case, the predictions are better than that by the existing Chase and Frendi models.

A comparison of the turbulent pressure spectrum $\hat{p}_0(k_z, \omega)$ predicted by the hybrid model (Eqs. (13)-(18)), the Chase model (Eq. (1)) and the Frendi model (Eq. (9)) for different frequencies at 2 knots is shown in Fig. 3. Here, the diameter of the cylinder is chosen as 10 mm, density of the fluid is 1000 kg/m^3 and the SPL is calculated at 11 m from the leading edge of the solid cylinder. It can be seen from Fig. 3 that for a given frequency, at low wavenumbers, the turbulent pressure spectrum increases at a slow rate. It peaks at convective wavenumber $k_c (= \omega/u_c)$ forming a convective ridge. It can be seen that while all the models predict a ‘flat’ spectrum at lower wavenumbers and a ridge at convective wavenumber, their predictions differ significantly at large wavenumbers. The presence of an exponential function results in an exponential decrease in the spectrum at large wavenumbers for the hybrid and Frendi models. Chase model predicts a higher spectrum with a smaller slope at large wavenumbers. It can be seen from Fig. 3 that the predictions by the three models are closer at lower frequencies. However, at high frequencies,

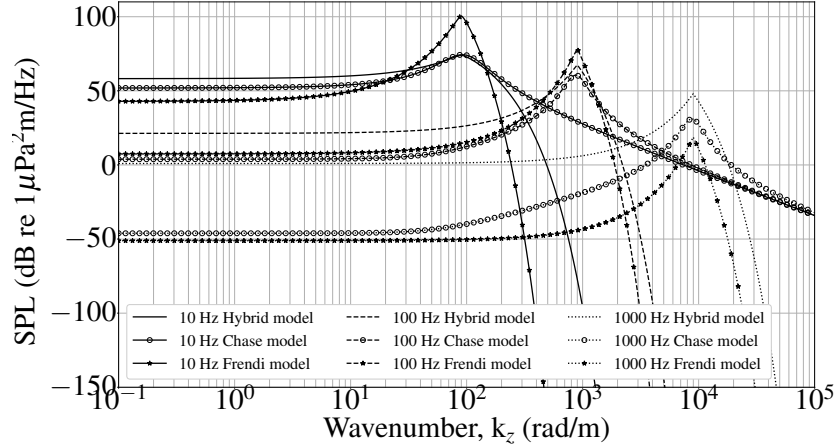


Fig. 3. A comparison of the turbulent pressure spectrum $\hat{p}_0(k_z, \omega)$ given by the hybrid model (Eq. (18)), Chase (Eq. (1)) and Frendi (Eq. (9)) model at 2 knots.

the hybrid model predicts a spectrum that is higher than the rest. This difference in the spectrum predicted by the hybrid model helps to achieve closer agreement with the measured flow noise, as shown in Fig. 2

2.3 Non-dimensional power spectral density

The non-dimensional power spectral density, Q_{ND} , of the flow noise is defined as

$$Q_{ND} = \frac{Q(\omega)}{\rho^2 D U^3}, \quad (19)$$

where $Q(\omega)$ is the flow noise given by Eq. (10) and D is the cylinder diameter. The non-dimensional power spectral density calculated using the hybrid model (Eqs. (13)-(18)) at different tow speeds are shown in Fig. 4.

It can be seen that, the non-dimensional power spectral density for different tow speeds collapse to a single curve against the non-dimensional frequency $\omega D/u$. One can therefore obtain the power spectral density at different tow speeds and cylinder diameters using this “single” non-dimensional curve.

While developing a new model of turbulent pressure field for axial flow past a solid cylinder, it is assumed that the cylinder is rigid and therefore the pressure field is not altered by the cylinder

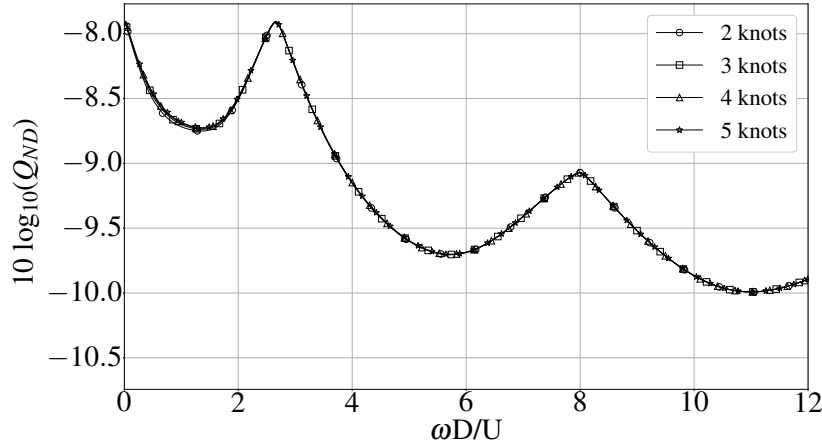


Fig. 4. Non-dimensional power spectral density for different tow speeds using the new hybrid model.

180 displacement field. However, the cylindrical tube in towed sonar arrays is not rigid and can be
 181 assumed to be elastic. The turbulent pressure fluctuation outside the elastic tube, creates vibration
 182 inside the tube and in turn generates acoustic waves in the fluid inside the tube. The following
 183 section presents a three-dimensional vibroacoustic model of a fluid-filled elastic tube, which is
 184 further used with the new hybrid model of the external turbulent pressure excitation to estimate
 185 on-axis flow noise.

3 THREE-DIMENSIONAL VIBROACOUSTIC (3D-VA) MODEL OF A FLUID-FILLED ELASTIC TUBE

186 This section develops a fully-coupled three-dimensional vibroacoustic (3D-VA) model of the
 187 fluid-filled elastic tube. A schematic of the fluid-filled tube is shown in Fig. 5. First, the displacement
 188 field of the elastic tube is derived from the Navier-Lame equilibrium equation (see Section 3.1) and
 189 then the acoustic pressure field inside the tube is derived from the acoustic wave equation (see
 190 Section 3.2). The structure (elastic tube) and the fluid (interior fluid) are then coupled with the
 191 help of stress and displacement boundary conditions at the interface (see Section 3.3). External
 192 pressure excitation is also taken into account in the form of a stress boundary condition on the
 193 outer surface of the tube. The boundary conditions, when expressed in terms of the unknown
 194 displacement and pressure fields, form a system of linear algebraic equations. The unknown
 195 displacement and pressure fields are then calculated by solving this system of equations (see

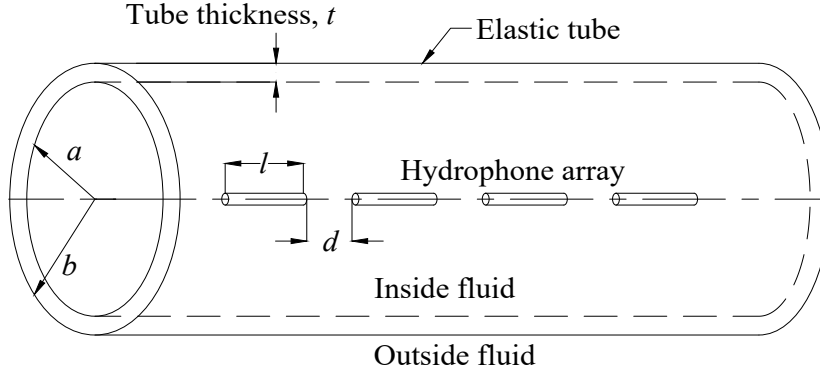


Fig. 5. Fluid filled elastic tube.

196 Section 3.4).

197 3.1 The elastic tube displacement and stress fields

198 This section involves modeling of an elastic tube using the Navier-Lame equilibrium equation in
 199 three-dimensional cylindrical coordinates. The Navier-Lame equilibrium equation is given by [15]

$$\mu \nabla^2 \mathbf{U}(r, \theta, z, t) + (\lambda + \mu) \nabla \nabla \cdot \mathbf{U}(r, \theta, z, t) = \rho_s \ddot{\mathbf{U}}(r, \theta, z, t), \quad (20)$$

200 where \mathbf{U} is the displacement vector ($= \{W_e, \Theta_e, U_e\}^T$, W_e represents the radial, Θ_e represents
 201 the azimuthal and U_e , the axial displacement fields), λ and μ are the Lamé's coefficients, ρ_s is the
 202 density of the tube and ∇ is the gradient operator in three dimension given by

$$\nabla = \frac{\partial}{\partial r} \mathbf{e}_r + \frac{1}{r} \frac{\partial}{\partial \theta} \mathbf{e}_\theta + \frac{\partial}{\partial z} \mathbf{e}_z. \quad (21)$$

203 The displacement vector \mathbf{U} may be represented using the Helmholtz decomposition method as

$$\mathbf{U} = \nabla \phi + \nabla \times \boldsymbol{\psi}, \quad (22)$$

204 where ϕ is a scalar potential and ψ is a vector potential. The scalar and vector potential functions
 205 satisfy the Navier-Lame equation for $n = 0$ and for all positive integer values of n . A complete
 206 solution to Navier-Lame equation can be obtained as

$$\phi(r, \theta, z, t) = \sum_{n=0}^{\infty} [A_1 J_n(\beta_1 r) + A_2 Y_n(\beta_1 r)] [A_3 \cos(n\theta) + A_4 \sin(n\theta)] e^{i(k_z z - \omega t)}, \quad (23)$$

207

$$\psi_r(r, \theta, z, t) = \sum_{n=0}^{\infty} [C_1 J_{n+1}(\beta_2 r) + C_2 Y_{n+1}(\beta_2 r)] \sin(n\theta) e^{i(k_z z - \omega t)}, \quad (24)$$

208

$$\psi_\theta(r, \theta, z, t) = \sum_{n=0}^{\infty} -[C_1 J_{n+1}(\beta_2 r) + C_2 Y_{n+1}(\beta_2 r)] \cos(n\theta) e^{i(k_z z - \omega t)} \quad (25)$$

209 and

$$\psi_z(r, \theta, z, t) = \sum_{n=0}^{\infty} [B_1 J_n(\beta_2 r) + B_2 Y_n(\beta_2 r)] [B_3 \cos(n\theta) + B_4 \sin(n\theta)] e^{i(k_z z - \omega t)} \quad (26)$$

210 In this work, the above expressions are truncated to only $n = 0$ and $n = 1$ terms and further used
 211 to compute the elastic tube displacement and stress fields. A detailed derivation of the potential
 212 functions are given in Section S1 of the Supplemental material.

213 3.1.1 Elastic tube displacement components

214 In this subsection, the displacement components of the elastic tube in radial (W_e), azimuthal
215 (Θ_e) and axial (U_e) directions, are derived. The displacement components are given by Eq. (22).

$$W_e(r, \theta, z, t) = \frac{\partial \phi}{\partial r} + \frac{1}{r} \frac{\partial \psi_z}{\partial \theta} - \frac{\partial \psi_\theta}{\partial z}, \quad (27)$$

216

$$\Theta_e(r, \theta, z, t) = \frac{1}{r} \frac{\partial \phi}{\partial \theta} + \frac{\partial \psi_r}{\partial z} - \frac{\partial \psi_z}{\partial r} \quad (28)$$

217 and

$$U_e(r, \theta, z, t) = \frac{\partial \phi}{\partial r} + \frac{1}{r} \frac{\partial \psi_z}{\partial \theta} - \frac{\partial \psi_\theta}{\partial z} \quad (29)$$

218 Substituting for the scalar (Eq. (23)) and the vector potential (Eqs. (24) - (26)) functions, the radial
219 displacement field is

$$\begin{aligned} W_e(r, \theta, z, t) = & e^{i(k_z z - \omega t)} \left\{ \frac{1}{r} [r\beta_1 J_0(r\beta_1) \cos(\theta) - J_1(r\beta_1)(\cos(\theta) + r\beta_1)] E_1 + \frac{1}{r} \sin(\theta) [r\beta_1 J_0(r\beta_1) \right. \\ & - J_1(r\beta_1)] E_2 + \frac{1}{r} [r\beta_1 Y_0(r\beta_1) \cos(\theta) - Y_1(r\beta_1)(\cos(\theta) + r\beta_1)] F_1 + \frac{1}{r} \sin(\theta) [r\beta_1 Y_0(r\beta_1) \\ & - Y_1(r\beta_1)] F_2 + ik_z [J_1(r\beta_2) + J_2(r\beta_2) \cos(\theta)] G_1 + ik_z [J_1(r\beta_2) + J_2(r\beta_2) \cos(\theta)] G_2 \\ & \left. + [\frac{1}{r} J_1(r\beta_2) \cos(\theta)] H_1 + [\frac{1}{r} Y_1(r\beta_2) \cos(\theta)] H_2 - [\frac{1}{r} J_1(r\beta_2) \sin(\theta)] I_1 - [\frac{1}{r} Y_1(r\beta_2) \sin(\theta)] I_2 \right\}, \quad (30) \end{aligned}$$

220 where, $E_1, E_2, F_1, F_2, G_1, G_2, H_1, H_2, I_1$ and I_2 are unknown constants with $E_1 = A_1 A_3, E_2 =$
221 $A_1 A_4, F_1 = A_2 A_3, F_2 = A_2 A_4, G_1 = C_1, G_2 = C_2, H_1 = B_1 B_4, H_2 = B_2 B_4, I_1 = B_1 B_3$ and

222 $I_2 = B_2 B_3$. The azimuthal displacement field is

$$\begin{aligned} \Theta_e(r, \theta, z, t) = & \mathbf{e}^{i(k_z z - \omega t)} \left\{ \frac{-1}{r} [J_1(r\beta_1) \sin(\theta)] E_1 + \frac{1}{r} [J_1(r\beta_1) \cos(\theta)] E_2 + \frac{-1}{r} [Y_1(r\beta_1) \sin(\theta)] F_1 \right. \\ & + \frac{1}{r} [Y_1(r\beta_1) \cos(\theta)] F_2 + [ik_z J_2(r\beta_2) \sin(\theta)] G_1 + [ik_z Y_2(r\beta_2) \sin(\theta)] G_2 \\ & - \frac{\beta_2 \sin(\theta)}{2} [J_0(r\beta_2) - J_2(r\beta_2)] H_1 - \frac{\beta_2 \sin(\theta)}{2} [Y_0(r\beta_2) - Y_2(r\beta_2)] H_2 \\ & + \frac{1}{r} \{-r\beta_2 J_0(r\beta_2) \cos(\theta) + J_1(r\beta_2) [r\beta_2 + \cos(\theta)]\} I_1 + \frac{1}{r} \{-r\beta_2 Y_0(r\beta_2) \cos(\theta) \\ & \left. + Y_1(r\beta_2) [r\beta_2 + \cos(\theta)]\} I_2 \right\}. \quad (31) \end{aligned}$$

223 The axial displacement field is

$$\begin{aligned} U_e(r, \theta, z, t) = & \mathbf{e}^{i(k_z z - \omega t)} \left\{ ik_z [J_0(r\beta_1) + J_1(r\beta_1) \cos(\theta)] E_1 + [ik_z J_1(r\beta_1) \sin(\theta)] E_2 \right. \\ & + ik_z [Y_0(r\beta_1) + Y_1(r\beta_1) \cos(\theta)] F_1 + [ik_z Y_1(r\beta_1) \sin(\theta)] F_2 \\ & \left. - \beta_2 [J_0(r\beta_2) + J_1(r\beta_2) \cos(\theta)] G_1 - \beta_2 [Y_0(r\beta_2) + Y_1(r\beta_2) \cos(\theta)] G_2 \right\}. \quad (32) \end{aligned}$$

224 The spatio-temporal (r, θ, z, t) displacement field is then transformed to the wavenumber-frequency

225 (r, θ, k_z, ω) domain using the Fourier transform pairs,

$$\hat{G}(r, \theta, k_z, \omega) = \frac{1}{4\pi^2} \int_{-\infty}^{\infty} \int_{-\infty}^{\infty} g(r, \theta, z, t) e^{-i(k_z z - \omega t)} dz dt, \quad (33)$$

and

$$g(r, \theta, z, t) = \int_{-\infty}^{\infty} \int_{-\infty}^{\infty} \hat{G}(r, \theta, k_z, \omega) \mathbf{e}^{i(k_z z - \omega t)} dk_z d\omega. \quad (34)$$

226 The transformed displacement components are given below.

227 (a) Radial displacement:

$$\begin{aligned} \hat{W}_e(r, \theta, k_z, \omega) = & \left\{ \frac{-\chi_1}{2} \{2J_1(r\beta_1) + [J_2(r\beta_1) - J_0(r\beta_1)] \cos(\theta)\} \right\} \hat{P}_1(k_z, \omega) \\ & + \left\{ \frac{\chi_1}{2} [J_0(r\beta_1) - J_2(r\beta_1)] \sin(\theta) \right\} \hat{P}_2(k_z, \omega) + \left\{ \frac{-\chi_1}{2} \{2Y_1(r\beta_1) \right. \\ & + [Y_2(r\beta_1) - Y_0(r\beta_1)] \cos(\theta)\} \right\} \hat{Q}_1(k_z, \omega) + \left\{ \frac{\chi_1}{2} [Y_0(r\beta_1) - Y_2(r\beta_1)] \sin(\theta) \right\} \hat{Q}_2(k_z, \omega) \\ & - \left\{ \chi_2 [J_1(r\beta_2) + J_2(r\beta_2) \cos(\theta)] \right\} \hat{R}_1(k_z, \omega) - \left\{ \chi_2 [Y_1(r\beta_2) + Y_2(r\beta_2) \cos(\theta)] \right\} \hat{R}_2(k_z, \omega) \\ & + \left\{ \frac{1}{r} [J_1(r\beta_2) \cos(\theta)] \right\} \hat{S}_1(k_z, \omega) + \left\{ \frac{1}{r} [Y_1(r\beta_2) \cos(\theta)] \right\} \hat{S}_2(k_z, \omega) \\ & + \left\{ \frac{1}{r} [J_1(r\beta_2) \sin(\theta)] \right\} \hat{T}_1(k_z, \omega) + \left\{ \frac{1}{r} [Y_1(r\beta_2) \sin(\theta)] \right\} \hat{T}_2(k_z, \omega), \quad (35) \end{aligned}$$

228 where $\hat{P}_1(k_z, \omega)$, $\hat{P}_2(k_z, \omega)$, $\hat{Q}_1(k_z, \omega)$, $\hat{Q}_2(k_z, \omega)$, $\hat{R}_1(k_z, \omega)$, $\hat{R}_2(k_z, \omega)$, $\hat{S}_1(k_z, \omega)$, $\hat{S}_2(k_z, \omega)$, $\hat{T}_1(k_z, \omega)$

229 and $\hat{T}_2(k_z, \omega)$ are the unknown variables and $\chi_1 = \frac{\beta_1}{jk_z}$ and $\chi_2 = \frac{jk_z}{\beta_2}$.

230 (b) Azimuthal displacement:

$$\begin{aligned} \hat{\Theta}_e(r, \theta, k_z, \omega) = & \left\{ \frac{-\chi_1}{r\beta_1} [J_1(r\beta_1) \sin(\theta)] \right\} \hat{P}_1(k_z, \omega) + \left\{ \frac{\chi_1}{r\beta_1} [J_1(r\beta_1) \cos(\theta)] \right\} \hat{P}_2(k_z, \omega) \\ & + \left\{ \frac{-\chi_1}{r\beta_1} [Y_1(r\beta_1) \sin(\theta)] \right\} \hat{Q}_1(k_z, \omega) + \left\{ \frac{\chi_1}{r\beta_1} [Y_1(r\beta_1) \cos(\theta)] \right\} \hat{Q}_2(k_z, \omega) \\ & - \left\{ \chi_2 J_2(r\beta_2) \sin(\theta) \right\} \hat{R}_1(k_z, \omega) - \left\{ \chi_2 Y_2(r\beta_2) \sin(\theta) \right\} \hat{R}_2(k_z, \omega) \\ & + \left\{ \frac{\sin(\theta)}{r} [J_1(r\beta_2) - r\beta_2 J_0(r\beta_2)] \right\} \hat{S}_1(k_z, \omega) + \left\{ \frac{\sin(\theta)}{r} [Y_1(r\beta_2) - r\beta_2 Y_0(r\beta_2)] \right\} \hat{S}_2(k_z, \omega) \\ & + \left\{ \beta_2 J_0(r\beta_2) \cos(\theta) - \frac{1}{r} \{J_1(r\beta_2) * [r\beta_2 + \cos(\theta)]\} \right\} \hat{T}_1(k_z, \omega) \end{aligned}$$

$$+ \left\{ \beta_2 Y_0(r\beta_2) \cos(\theta) - \frac{1}{r} \{Y_1(r\beta_2) * [r\beta_2 + \cos(\theta)]\} \right\} \hat{T}_2(k_z, \omega) \quad (36)$$

231 (c) Axial displacement:

$$\begin{aligned} \hat{U}_e(r, \theta, k_z, \omega) = & \left\{ J_0(r\beta_1) + J_1(r\beta_1) \cos(\theta) \right\} \hat{P}_1(k_z, \omega) + \left\{ J_1(r\beta_1) \sin(\theta) \right\} \hat{P}_2(k_z, \omega) \\ & + \left\{ Y_0(r\beta_1) + Y_1(r\beta_1) \cos(\theta) \right\} \hat{Q}_1(k_z, \omega) + \left\{ Y_1(r\beta_1) \sin(\theta) \right\} \hat{Q}_2(k_z, \omega) \\ & + \left\{ J_0(r\beta_2) + J_1(r\beta_2) \cos(\theta) \right\} \hat{R}_1(k_z, \omega) + \left\{ Y_0(r\beta_2) + Y_1(r\beta_2) \cos(\theta) \right\} \hat{R}_2(k_z, \omega). \end{aligned} \quad (37)$$

232 The unknown variables in the displacement components, are related to the unknown constants

233 $A_1, A_2, A_3, A_4, B_1, B_2, B_3, B_4, C_1$ and C_2 in the potential functions as,

$$\hat{P}_1(k_z, \omega) = 2\pi i A_1 A_3 k_z \delta(k + k_z) \delta(\omega - \omega_0), \quad (38)$$

$$\hat{P}_2(k_z, \omega) = 2\pi i A_2 A_3 k_z \delta(k + k_z) \delta(\omega - \omega_0), \quad (39)$$

$$\hat{Q}_1(k_z, \omega) = 2\pi i A_1 A_4 k_z \delta(k + k_z) \delta(\omega - \omega_0), \quad (40)$$

$$\hat{Q}_2(k_z, \omega) = 2\pi i A_2 A_4 k_z \delta(k + k_z) \delta(\omega - \omega_0), \quad (41)$$

$$\hat{R}_1(k_z, \omega) = -2\pi C_1 \beta_1 \delta(k + k_z) \delta(\omega - \omega_0), \quad (42)$$

$$\hat{R}_2(k_z, \omega) = -2\pi C_2 \beta_1 \delta(k + k_z) \delta(\omega - \omega_0), \quad (43)$$

$$\hat{S}_1(k_z, \omega) = 2\pi B_1 B_4 \delta(k + k_z) \delta(\omega - \omega_0), \quad (44)$$

$$\hat{S}_2(k_z, \omega) = 2\pi B_2 B_4 \delta(k + k_z) \delta(\omega - \omega_0), \quad (45)$$

$$\hat{T}_1(k_z, \omega) = -2\pi B_1 B_3 \delta(k + k_z) \delta(\omega - \omega_0), \quad (46)$$

234 and

$$\hat{T}_2(k_z, \omega) = -2\pi B_2 B_3 \delta(k + k_z) \delta(\omega - \omega_0), \quad (47)$$

235 where $\delta()$ is the dirac delta function. In the above equations (Eqs. (38)-(47)), two unknown vari-
236 ables can be expressed in terms of other variables as,

$$\hat{Q}_2(k_z, \omega) = \frac{\hat{P}_2(k_z, \omega) \hat{Q}_1(k_z, \omega)}{\hat{P}_1(k_z, \omega)} \text{ and } \hat{T}_2(k_z, \omega) = \frac{\hat{S}_2(k_z, \omega) \hat{T}_1(k_z, \omega)}{\hat{S}_1(k_z, \omega)}. \quad (48)$$

237 Thus, of the ten unknown variables (Eqs. (38)-(47)), present in the displacement fields (Eqs. (35)
238 - (37)), only eight are independent.

239 3.1.2 Elastic stress components

240 The elastic tube and the acoustic fluid inside the tube are coupled through displacement and
241 stress boundary conditions. Of all the stress components, only τ_{rr} , $\tau_{r\theta}$, τ_{rz} , and $\tau_{z\theta}$ are of interest
242 to us. These components may be computed using the constitutive relations [15]. They are,

$$\tau_{rr}(r, \theta, z, t) = (\lambda + 2\mu) \frac{\partial W_e}{\partial r} + \frac{\lambda}{r} \left(W_e + \frac{\partial \Theta_e}{\partial \theta} \right) + \lambda \frac{\partial U_e}{\partial z}, \quad (49)$$

243

$$\tau_{rz}(r, \theta, z, t) = \mu \left(\frac{\partial W_e}{\partial z} + \frac{\partial U_e}{\partial r} \right), \quad (50)$$

244

$$\tau_{r\theta}(r, \theta, z, t) = \mu \left(\frac{1}{r} \frac{\partial W_e}{\partial \theta} + \frac{\partial \Theta_e}{\partial r} - \frac{\Theta_e}{r} \right), \quad (51)$$

245 and

$$\tau_{z\theta}(r, \theta, z, t) = \mu \left(\frac{\partial \Theta_e}{\partial z} + \frac{1}{r} \frac{\partial U_e}{\partial \theta} \right). \quad (52)$$

246 The constitutive relations above are transformed into the frequency - wavenumber ($\omega - k_z$) domain
 247 using the Fourier transform pair (Eqs. (33) and (34)). Furthermore, displacement components
 248 derived in the previous subsection are substituted to obtain closed form expressions for these
 249 stress components (see Eqs. (S.40), (S.44), (S.45) and (S.46) in the supplemental material). A
 250 detailed derivation of the stress components using the constitutive relations are given in Section S2
 251 in supplemental material.

252 3.2 The interior fluid acoustic pressure and displacement fields

253 The interior fluid is assumed to be confined inside an infinitely long elastic tube. The acoustic
 254 wave propagation in the fluid is governed by

$$\nabla^2 p_f(r, \theta, z, t) = \frac{1}{c_a^2} \frac{\partial^2 p_f(r, \theta, z, t)}{\partial t^2}, \quad (53)$$

255 where p_f is the acoustic pressure, c_a is the speed of sound in the fluid inside the tube and ∇^2 is
 256 the Laplacian. In cylindrical coordinates,

$$\nabla^2 = \frac{\partial^2}{\partial r^2} + \frac{1}{r} \frac{\partial}{\partial r} + \frac{1}{r^2} \frac{\partial^2}{\partial \theta^2} + \frac{\partial^2}{\partial z^2}. \quad (54)$$

257 Assuming a plane wave propagation in the z direction and using a variable separable form for p_f ,

$$p_f(r, \theta, z, t) = R(r)\Theta(\theta)e^{j(k_z z - \omega t)}. \quad (55)$$

258 Substituting Eq. (55) in Eq. (53), and rearranging gives

$$\frac{r^2}{R} \frac{\partial^2 R(r)}{\partial r^2} + \frac{r}{R} \frac{\partial R(r)}{\partial r} + \alpha^2 r^2 = -\frac{1}{\Theta} \frac{\partial^2 \Theta}{\partial \theta^2}, \quad (56)$$

259 where $\alpha^2 = \frac{\omega^2}{c_a^2} - k_z^2$. For the above equation, only those solutions are valid for which the left hand

260 side and the right hand sides are equal to a positive constant (n^2). Therefore,

$$\frac{r^2}{R} \frac{\partial^2 R(r)}{\partial r^2} + \frac{r}{R} \frac{\partial R(r)}{\partial r} + \alpha^2 r^2 = -\frac{1}{\Theta} \frac{\partial^2 \Theta}{\partial \theta^2} = n^2. \quad (57)$$

261 From the above equation, $\Theta(\theta)$ can be obtained by solving

$$\frac{\partial^2 \Theta}{\partial \theta^2} + n^2 \Theta = 0. \quad (58)$$

262 A general solution to Eq. (58) is

$$\Theta(\theta) = P_{f01} \cos(n\theta) + P_{f02} \sin(n\theta), \quad (59)$$

263 where P_{f01} and P_{f02} are unknowns. Similarly from Eq. (57), $R(r)$ is governed by,

$$\frac{\partial^2 R}{\partial r^2} + \frac{1}{r} \frac{\partial R}{\partial r} + \left(\alpha^2 - \frac{n^2}{r^2} \right) R = 0. \quad (60)$$

264 A general solution to Eq. (60) is

$$R(r) = P_{f03} J_n(\alpha r) + P_{f04} Y_n(\alpha r), \quad (61)$$

265 where P_{f03} and P_{f04} are unknowns. As $r \rightarrow 0$, $Y_n(\alpha r) \rightarrow -\infty$, the second term on the right hand
 266 side must vanish for all valid pressure fields inside a cylindrical tube. Therefore, $P_{f04} = 0$. Thus,
 267 using Eqs. (55), (59) and (61),

$$p_f(r, \theta, z, t) = P_{f03} J_n(\alpha r) [P_{f01} \cos(n\theta) + P_{f02} \sin(n\theta)] e^{j(k_z z - \omega t)} \quad (62)$$

268 The above equation is valid for $n = 0, 1, 2, \dots$ etc. A complete solution to the acoustic pressure field
 269 may be written as,

$$p_f(r, \theta, z, t) = \sum_{n=0}^{\infty} P_{f03} J_n(\alpha r) [P_{f01} \cos(n\theta) + P_{f02} \sin(n\theta)] e^{j(k_z z - \omega t)} \quad (63)$$

270 Only $n = 0$ and $n = 1$ terms in Eq. (63) are considered in this work. Further, Eq. (63) is transformed
 271 to the frequency-wavenumber ($\omega - k_z$) domain using Eq. (33) and is given by

$$\hat{p}_f(r, \theta, k_z, \omega) = \hat{P}_{f1}(k_z, \omega) [J_0(\alpha r) + J_1(\alpha r) \cos(\theta)] + \hat{P}_{f2}(k_z, \omega) J_1(\alpha r) \sin(\theta), \quad (64)$$

272 where $\hat{P}_{f1}(k_z, \omega)$ and $\hat{P}_{f2}(k_z, \omega)$ are two unknowns, which are function of the constants P_{f01} , P_{f02}
 273 and P_{f03} . They are related as,

$$\hat{P}_{f1}(k_z, \omega) = 2\pi P_{f03} P_{f01} \delta(k + k_z) \delta(\omega - \omega_0) \quad (65)$$

274 and

$$\hat{P}_{f2}(k_z, \omega) = 2\pi P_{f03} P_{f02} \delta(k + k_z) \delta(\omega - \omega_0). \quad (66)$$

275 The acoustic particle velocity in the radial, azimuthal and axial directions can be obtained with the
276 help of Euler equation,

$$\nabla p_f(r, \theta, z, t) = -\rho \frac{\partial \mathbf{u}_f(r, \theta, z, t)}{\partial t}, \quad (67)$$

277 where ∇ is the gradient operator and \mathbf{u}_f is the acoustic particle velocity. The acoustic fluid particle
278 velocity \mathbf{u}_f may be represented as,

$$\mathbf{u}_f(r, \theta, z, t) = u_{fr}(r, \theta, z, t)\mathbf{e}_r + u_{f\theta}(r, \theta, z, t)\mathbf{e}_\theta + u_{fz}(r, \theta, z, t)\mathbf{e}_z, \quad (68)$$

279 where u_{fr} , $u_{f\theta}$ and u_{fz} are the radial, azimuthal and axial components of the fluid particle velocity,
280 respectively. In the above equation, as for the acoustic pressure, a harmonic variation in the form
281 of $e^{j(k_z z - \omega t)}$ is assumed for the particle velocity. Substituting for \mathbf{u}_f (Eq. (68)) and transforming to
282 the frequency-wavenumber domain, Eq. (67) results

$$\begin{aligned} \frac{\partial \hat{p}_f(r, \theta, k_z, \omega)}{\partial r} \mathbf{e}_r + \frac{1}{r} \frac{\partial \hat{p}_f(r, \theta, k_z, \omega)}{\partial \theta} \mathbf{e}_\theta + \frac{\partial \hat{p}_f(r, \theta, k_z, \omega)}{\partial z} \mathbf{e}_z \\ = j\rho\omega \hat{u}_{fr}(r, \theta, k_z, \omega) \mathbf{e}_r + j\rho\omega \hat{u}_{f\theta}(r, \theta, k_z, \omega) \mathbf{e}_\theta + j\rho\omega \hat{u}_{fz}(r, \theta, k_z, \omega) \mathbf{e}_z. \end{aligned} \quad (69)$$

283 3.2.1 Radial component of the fluid particle displacement

284 Comparing and equating the radial components on the left and right hand sides of Eq. (69)
285 result in

$$\frac{\partial \hat{p}_f(r, \theta, k_z, \omega)}{\partial r} = j\rho\omega \hat{u}_{fr}(r, \theta, k_z, \omega) \quad (70)$$

286 Substituting for the acoustic pressure $\hat{p}_f(r, \theta, k_z, \omega)$ from Eq. (64) and simplifying yields

$$\begin{aligned} \hat{u}_{fr}(r, \theta, k_z, \omega) = \frac{1}{j\rho\omega} \left\{ \alpha J_0(r\alpha) \cos(\theta) - \frac{J_1(r\alpha)}{r} [r\alpha + \cos(\theta)] \right\} \hat{P}_{f1} \\ + \frac{1}{j\rho\omega} \left\{ \frac{\alpha \sin(\theta)}{2} [J_0(r\alpha) - J_2(r\alpha)] \right\} \hat{P}_{f2}. \end{aligned} \quad (71)$$

287 Let U_{fr} be the radial displacement of the fluid particle, defined by

$$U_{fr}(r, \theta, z, t) = \tilde{U}_{fr}(r, \theta) e^{j(k_z z - \omega t)}. \quad (72)$$

288 In the frequency-wavenumber domain, the fluid particle displacement and velocity in the radial
289 direction are related as

$$\hat{U}_{fr}(r, \theta, k_z, \omega) = \frac{j}{\omega} \hat{u}_{fr}(r, \theta, k_z, \omega). \quad (73)$$

290 Substituting for $\hat{u}_{fr}(r, \theta, k_z, \omega)$ (Eq. (71)) in the above equation, the radial component of the fluid
291 particle displacement is given by

$$\begin{aligned} \hat{U}_{fr}(r, \theta, k_z, \omega) = \left\{ \frac{1}{r\rho\omega^2} \{ r\alpha J_0(r\alpha) \cos(\theta) - J_1(r\alpha) [r\alpha + \cos(\theta)] \} \right\} \hat{P}_{f1} \\ + \left\{ \frac{\sin(\theta)}{r\rho\omega^2} [r\alpha J_0(r\alpha) - J_1(r\alpha)] \right\} \hat{P}_{f2}. \end{aligned} \quad (74)$$

292 3.2.2 Azimuthal component of the fluid particle displacement

293 Comparing and equating the azimuthal components on the left and right hand sides of Eq. (69)

294 result in

$$\frac{1}{r} \frac{\partial \hat{p}_f(r, \theta, k_z, \omega)}{\partial \theta} = j \rho \omega \hat{u}_{f\theta}(r, \theta, k_z, \omega) \quad (75)$$

295 Substituting for the acoustic pressure $\hat{p}_f(r, \theta, k_z, \omega)$ from Eq. (64) and simplifying yields

$$\hat{u}_{f\theta}(r, \theta, k_z, \omega) = \left\{ \frac{1}{r \rho \omega} [j \sin(\theta) J_1(r\alpha)] \right\} \hat{P}_{f1} + \left\{ \frac{-1}{r \rho \omega} [j \cos(\theta) J_1(r\alpha)] \right\} \hat{P}_{f2}. \quad (76)$$

296 Let $U_{f\theta}$ be the azimuthal displacement of the fluid particle defined by

$$U_{f\theta}(r, \theta, z, t) = \tilde{U}_{f\theta}(r, \theta) e^{j(k_z z - \omega t)}. \quad (77)$$

297 In the frequency-wavenumber domain, the fluid particle displacement and velocity in the azimuthal

298 directions are related as

$$\hat{U}_{f\theta}(r, \theta, k_z, \omega) = \frac{j}{\omega} \hat{u}_{f\theta}(r, \theta, k_z, \omega). \quad (78)$$

299 Substituting for $\hat{u}_{f\theta}(r, \theta, k_z, \omega)$ (Eq. (76)) in the above equation, the azimuthal component of the

300 fluid particle displacement is given by

$$\hat{U}_{f\theta}(r, \theta, k_z, \omega) = \left\{ \frac{-1}{r \rho \omega^2} [J_1(r\alpha) \sin(\theta)] \right\} \hat{P}_{f1} + \left\{ \frac{1}{r \rho \omega^2} [J_1(r\alpha) \cos(\theta)] \right\} \hat{P}_{f2}. \quad (79)$$

3.3 Boundary conditions

The field variables derived in the previous subsections involve unknown variables. It is shown in Section 3.1 that the elastic tube displacement (Eqs. (35), (36) and (37)) and stress (Eqs. (49), (50), (51) and (52)) fields have eight unknowns: \hat{P}_1 , \hat{P}_2 , \hat{Q}_1 , \hat{R}_1 , \hat{R}_2 , \hat{S}_1 , \hat{S}_2 and \hat{T}_1 . Section 3.2 shows that the interior fluid pressure (Eq. (64)) and the fluid particle displacement fields (Eqs. (74) and (79)) have two unknowns: \hat{P}_{f1} and \hat{P}_{f2} . These ten unknown variables can be calculated with the help of boundary conditions on the inner ($r = a$) and outer ($r = b$) surfaces of the elastic tube. This subsection discusses the ten boundary conditions that are used to compute the ten unknown variables. Note that in the previous subsection, all field variables are expressed in the $r - \theta - k_z - \omega$ domain. These closed form expressions are transformed numerically into the $r - k_\theta - k_z - \omega$ domain using the discrete Fourier transform pair given below before use in the boundary conditions.

$$\hat{G}(r, k_\theta, k_z, \omega) = \sum_{\theta=0}^{N-1} g(r, \theta, k_z, \omega) e^{-j2\pi k_\theta \theta / N} \quad (80)$$

$$g(r, \theta, k_z, \omega) = \frac{1}{N} \sum_{k_\theta=0}^{N-1} \hat{G}(r, k_\theta, k_z, \omega) e^{j2\pi k_\theta \theta / N} \quad (81)$$

The ten boundary conditions are given below.

1. On the interior surface of the elastic tube ($r = a$), the radial component of the normal stress τ_{rr} is equal to the negative of the acoustic pressure p_f . In the $k_\theta - k_z - \omega$ domain, this can be written as

$$\hat{\tau}_{rr}(a, k_\theta, k_z, \omega) = -\hat{p}_f(a, k_\theta, k_z, \omega) \quad (82)$$

2. On the exterior surface of the elastic tube ($r = b$), the radial component of the normal stress τ_{rr} is equal to the negative of the external turbulent pressure p_0 . In the $k_\theta - k_z - \omega$ domain,

318 this may be written as

$$\hat{\tau}_{rr}(b, k_\theta, k_z, \omega) = -\hat{p}_0(k_z, \omega) \quad (83)$$

319 where $\hat{p}_0(k_z, \omega)$ is assumed to be a function of k_z and ω alone and is given by Eq. (18) for the
 320 hybrid model. For cases where the external pressure varies with θ , an appropriate pressure
 321 spectrum $\hat{p}_0(k_\theta, k_z, \omega)$ must be used.

322 3. The exterior and interior surfaces of the elastic tube are assumed to be shear-free. Therefore
 323 $\tau_{rz}|_{r=a,b} = 0$, $\tau_{r\theta}|_{r=a,b} = 0$ and $\tau_{z\theta}|_{r=a,b} = 0$. In the $k_\theta - k_z - \omega$ domain, this may be written as

$$\hat{\tau}_{rz}(r = a, k_\theta, k_z, \omega) = 0, \quad (84)$$

$$\hat{\tau}_{rz}(r = b, k_\theta, k_z, \omega) = 0, \quad (85)$$

$$\hat{\tau}_{r\theta}(r = a, k_\theta, k_z, \omega) = 0, \quad (86)$$

$$\hat{\tau}_{r\theta}(r = b, k_\theta, k_z, \omega) = 0, \quad (87)$$

$$\hat{\tau}_{z\theta}(r = a, k_\theta, k_z, \omega) = 0, \quad (88)$$

and

$$\hat{\tau}_{z\theta}(r = b, k_\theta, k_z, \omega) = 0. \quad (89)$$

324 4. The radial (W_e) and azimuthal (Θ_e) components of the elastic tube displacements on the inte-
 325 rior surface ($r = a$) must be equal to the respective fluid particle displacement (U_{fr} and $U_{f\theta}$)
 326 at $r = a$. In the $k_\theta - k_z - \omega$ domain, this may be written as

$$\hat{U}_{fr}(a, k_\theta, k_z, \omega) = \hat{W}_e(a, k_\theta, k_z, \omega) \quad (90)$$

and

$$\hat{U}_{f\theta}(a, k_\theta, k_z, \omega) = \hat{\Theta}_e(a, k_\theta, k_z, \omega). \quad (91)$$

The expressions for the acoustic pressure, the fluid and the elastic tube displacement components, and the elastic tube stress components derived in the previous subsections are substituted in the above boundary conditions. The resulting equations are given in detail in Section S3 in the supplemental material.

3.4 Solution methodology

Previous section discussed the boundary conditions associated with the elastic tube displacements and the acoustic pressure variations inside and outside the elastic tube. These boundary conditions result in ten equations involving twelve unknown variables (see section S3 in the supplemental material). Of the twelve unknown variables, only ten are independent. A further simplification of the boundary condition to include only the ten independent unknowns are presented in section S4 in supplemental material. The resulting system of algebraic equations may be represented in a matrix form,

$$\mathbf{A}(r, k_\theta, k_z, \omega) \mathbf{x} = \mathbf{b}(r, k_\theta, k_z, \omega), \quad (92)$$

where \mathbf{A} is the coefficient matrix of order 10×10 , \mathbf{x} is the unknown variable vector of order 10×1 and \mathbf{b} is the constant vector of order 10×1 . A detailed representation of \mathbf{A} , \mathbf{x} and \mathbf{b} are given in section S4 in the supplemental material. Eq. (92) is solved numerically for the unknown variable vector \mathbf{x} and the solution is used to calculate the interior acoustic pressure field $\hat{p}_f(r, k_\theta, k_z, \omega)$. The acoustic pressure field $\hat{p}_f(r, k_\theta, k_z, \omega)$ is further used to compute (a) azimuthal variation in the acoustic pressure field inside the elastic tube, (b) on-axis flow noise spectrum, and (c) on-axis flow noise.

346 3.4.1 Azimuthal variation in the interior acoustic pressure field

347 The interior acoustic pressure field $\hat{p}_f(r, k_\theta, k_z, \omega)$ is first multiplied with the square of the hy-
 348 drophone response function $H(k_z)$ (Eq. (11)) and then integrated over the entire axial wavenumber
 349 domain to get

$$Q(r = a, k_\theta, f) = 4\pi \int_{-\infty}^{\infty} \hat{p}_f(r = a, \theta, k_z, \omega) |H(k_z)|^2 dk_z. \quad (93)$$

350 The factor 4π is used to account for the negative frequency and radian frequency measure [8,
 351 9, 12]. The azimuthal variation in $Q(r = a, \theta, f)$ may be computed using the inverse Fourier
 352 transform,

$$Q(r = a, \theta, f) = \frac{1}{N} \sum_{k_\theta=0}^{N-1} Q(r = a, k_\theta, f) e^{j2\pi k_\theta \theta / N}. \quad (94)$$

353 The azimuthal variation in acoustic pressure level at the tube inner surface is computed using

$$SPL(r = a, \theta, f) = 10 \log_{10} \left(\frac{|Q(a, \theta, f)|}{p_{ref}^2} \right), \quad (95)$$

354 where $p_{ref} = 1\mu Pa$ is the reference acoustic pressure in water.

355 3.4.2 On-axis flow noise spectrum level

356 The acoustic pressure field $\hat{p}_f(r, k_\theta, k_z, \omega)$ is integrated over the azimuthal wavenumbers to
 357 obtain the on-axis flow noise spectrum as a function of frequency (ω) and axial wavenumber (k_z).

$$\hat{p}_f(r = 0, k_z, \omega) = \int_{-\infty}^{\infty} \hat{p}_f(r = 0, k_\theta, k_z, \omega) dk_\theta. \quad (96)$$

358 The on-axis flow noise spectrum level can be calculated by

$$SPL(r = 0, k_z, \omega) = 10 \log_{10} \left(\frac{|\hat{p}_f(r = 0, k_z, \omega)|}{p_{ref}^2} \right). \quad (97)$$

359 3.4.3 On-axis flow noise

360 First, the on-axis flow noise spectrum is computed using Eq. (96). It is further multiplied with
361 the square of the hydrophone response function $H(k_z)$ (Eq. (11)) and integrated over the axial
362 wavenumbers k_z to obtain on-axis flow noise $Q(r = 0, f)$. Thus,

$$Q(r = 0, f) = 4\pi \int_{-\infty}^{\infty} \hat{p}_f(r = 0, k_z, \omega) |H(k_z)|^2 dk_z. \quad (98)$$

363 The on-axis flow noise level can be computed using

$$SPL(r = 0, f) = 10 \log_{10} \left(\frac{|Q(r = 0, f)|}{p_{ref}^2} \right). \quad (99)$$

4 RESULTS AND DISCUSSIONS

364 Previous sections discussed the development of a fully-coupled three-dimensional vibroacous-
365 tic (3D-VA) model of a fluid-filled elastic tube under external pressure excitations. In this section,
366 the 3D-VA model is used to estimate the interior acoustic pressure field and flow noise in towed
367 sonar arrays. Section 4.1 presents the interior acoustic pressure field for azimuthally varying ex-
368 ternal pressure excitation over the fluid-filled elastic tube. Section 4.2 discusses the on-axis flow
369 noise spectrum due to an external turbulent pressure excitation. External turbulent pressure exci-
370 tation is computed using the hybrid model developed in this work (see Section 2). The results are
371 then compared with those obtained using the tube transfer function [9] and the axisymmetric vi-
372 broacoustic [11, 16] models available in the literature. Section 4.3 presents the on-axis flow noise
373 computed using the 3D-VA model and further compares the results with those predicted using

374 tube transfer function [9] and the axisymmetric [11] models. Further, Section 4.4 discusses the
 375 flow noise variation for various elastic tube diameters at different tow speeds.

376 4.1 Interior acoustic pressure field for azimuthally varying external excitation

377 The developed 3D-VA model of the fluid-filled elastic tube is initially tested with an exterior har-
 378 monic pressure excitation that has a known azimuthal variation. Results for two different external
 379 pressure excitation are presented here : (a) $\hat{p}_0(\theta, k_z) = \sin(\theta)$ (see Fig. 6) and (b) $\hat{p}_0(\theta, k_z) = \cos(\theta)$
 380 (see Fig. 7).

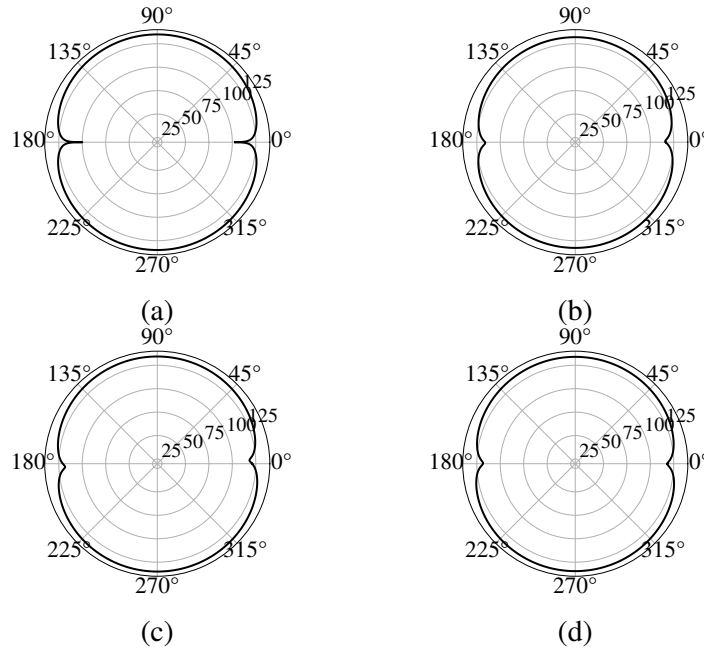


Fig. 6. (a): Azimuthal variation in the exterior pressure field $\hat{p}_0(\theta, k_z) = \sin(\theta)$. (b), (c) and (d): Azimuthal variation in the interior pressure field ($r = a$) at 10 Hz, 100 Hz and 1000 Hz, respectively, for $\hat{p}_0(\theta, k_z) = \sin(\theta)$.

381 Fig. 6(a) shows the azimuthal variation in the acoustic pressure (see Eqs. (93) - (95) with \hat{p}_f
 382 being replaced with $\sin(\theta)$) at the outer surface of the elastic tube. Figs. 6(b) - 6(d) shows the
 383 resulting azimuthal variation in the acoustic pressure at the inner surface ($r=a$) of the elastic tube
 384 for (b): 10 Hz, (c) 100 Hz and (d) 1000 Hz. Fig. 7 shows similar results for $\hat{p}_0(\theta, k_z) = \cos(\theta)$. The
 385 Figs. 6 and 7 confirms that the 3D-VA model accurately captures the azimuthal variation (restricted
 386 to $n = 0$ and $n = 1$) in the external pressure excitation.

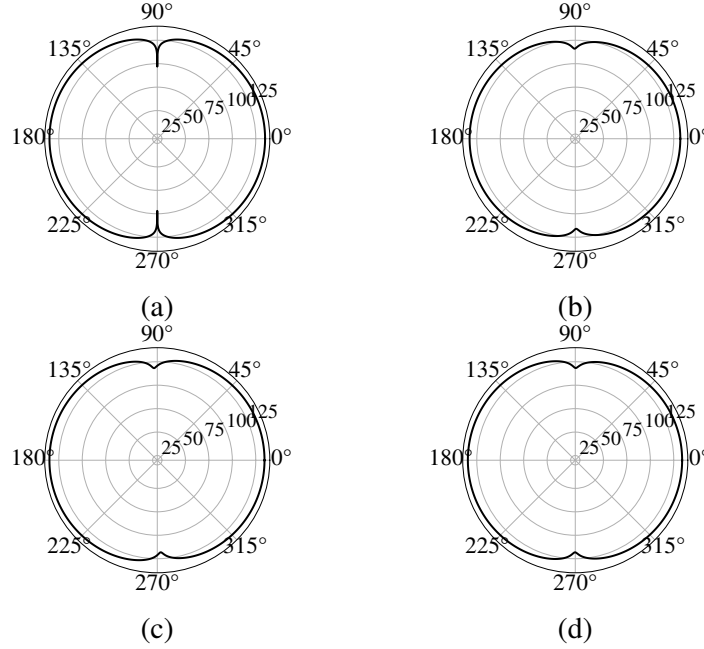


Fig. 7. (a): Azimuthal variation in the exterior pressure field $\hat{p}_0(\theta, k_z) = \cos(\theta)$. (b), (c) and (d): Azimuthal variation in the interior pressure field ($r = a$) at 10 Hz, 100 Hz and 1000 Hz, respectively, for $\hat{p}_0(\theta, k_z) = \cos(\theta)$.

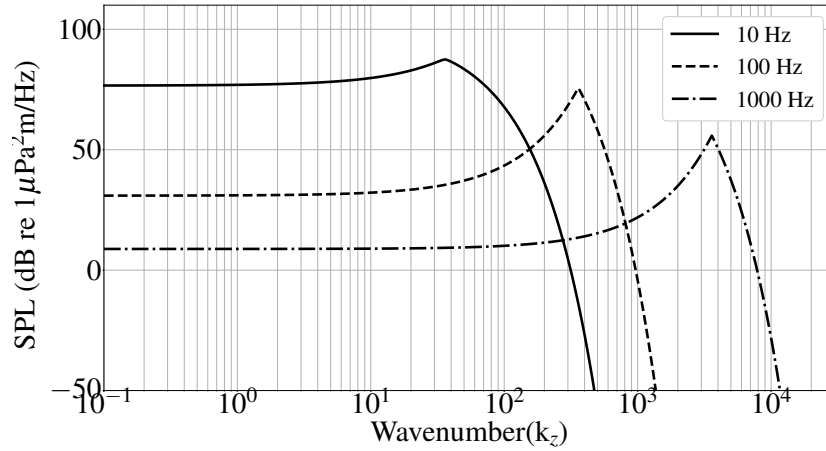


Fig. 8. The external turbulent pressure spectrum level computed using the hybrid model (Eq. (18)).

387 4.2 On-axis flow noise spectrum level for external turbulent pressure excitation

388 This section presents on-axis flow noise spectrum when the elastic tube is excited by an ex-
 389 ternal turbulent pressure field. The external turbulent pressure field (see Fig. 8) is computed using
 390 the hybrid model (Eq. (18)). Further, the 3D-VA model is used to calculate the on-axis flow noise
 391 spectrum (see Eqs. (96) and (97)). This flow noise spectrum is compared with that computed us-
 392 ing the tube transfer function model [9] (see Fig. 9) and the axisymmetric model [11] (see Fig. 10).

Table 1. The elastic tube, interior fluid and the hydrophone array parameters used for estimation of flow noise inside the cylinder

Property	Values
Tube diameter (m)	0.04
Tube thickness (m)	0.005
Tow speed/Flow velocity (knots)	5
Number of hydrophones	50
Length of hydrophone (m)	0.05
Hydrophone spacing (m)	0.25
Exterior fluid density (kg/m^3)	1000
Interior fluid density (kg/m^3)	800
Reference pressure (μPa)	1

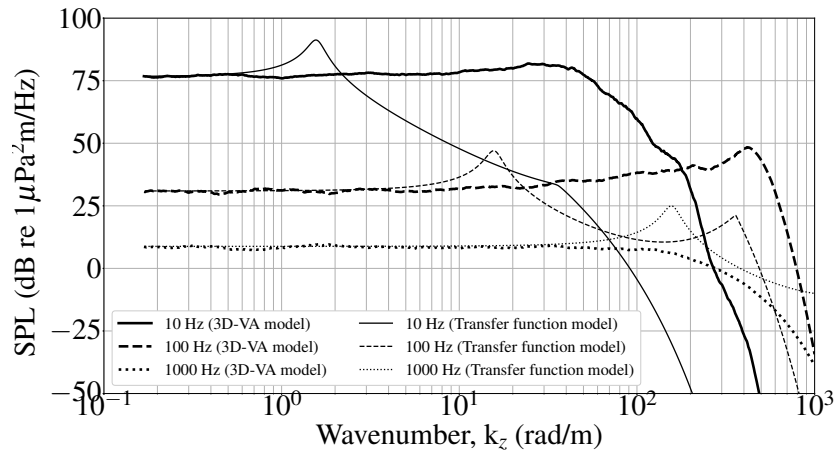


Fig. 9. Comparison of on-axis flow noise spectrum level due to a turbulent pressure excitation computed using the 3D-VA model and the tube transfer function model [9].

393 The elastic tube, inside fluid, and hydrophone array parameters used for computation are listed in
 394 Table 1. It can be seen from Figs. 9 and 10 that the on-axis acoustic pressure computed using the
 395 3D-VA model follows the external turbulent pressure excitation given in Fig. 8 - gradually increas-
 396 ing up to and peaking at the convective wavenumber ($u_c = \omega/k_c$), and decreasing exponentially
 397 beyond. Thus, the flow noise inside the tube is dominated by the contribution from wavenumbers
 398 less than the convective wavenumber.

399 In the tube transfer function model (Fig. 9) and the axisymmetric model (Fig. 10) predictions,

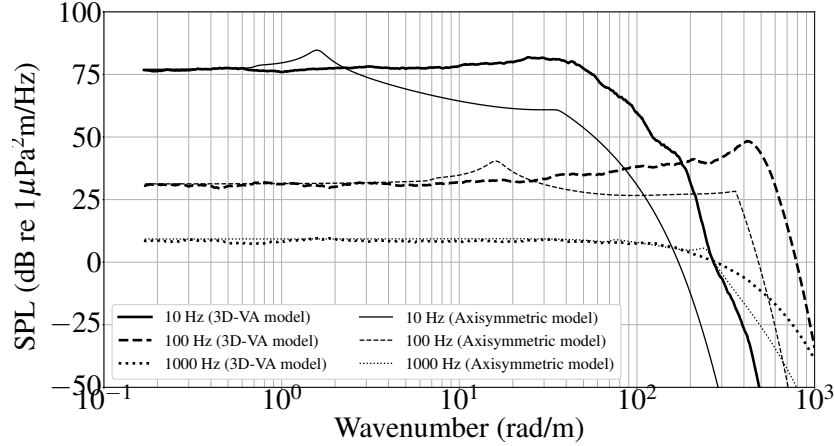


Fig. 10. Comparison of on-axis flow noise spectrum level due to a turbulent pressure excitation computed using the 3D-VA model and the axisymmetric model [11].

the peak occurs at a lower wavenumber than the convective wavenumber. For example, at 10 Hz, the peak occurs at 1.58 rad/m in the tube transfer function model and at 1.56 rad/m in the axisymmetric model. Note that the convective wavenumber at 10 Hz for 5 knots is $k_c = 35.93$ rad/m. This smaller wavenumber where the first peak occurs in the transfer function and the axisymmetric models corresponds to the breathing mode wavenumber, k_b , of the elastic tube given by [9]

$$k_b^2 = 2\rho_0\omega^2 R/Et. \quad (100)$$

In Eq. (100), ρ_0 is the density of the inside fluid, R is the outer radius of the elastic tube, E is the Young's modulus of the tube and t is the thickness of the tube. The tube transfer function model and the axisymmetric model consider only the breathing mode ($n = 0$) variations while modeling the fluid-filled elastic tube. The present 3D-VA model considers both $n = 0$ (breathing) and $n = 1$ (first order) variations in the solid and fluid displacement fields. The absence of peaks at the breathing wavenumber in the present 3D-VA model indeed demonstrates a cumulative effect of including both $n = 0$ and $n = 1$ order terms in the fully-coupled vibroacoustic formulation. The same is the reason for the difference in the flow noise spectrum between the 3D-VA model and the other models beyond the breathing wavenumber.

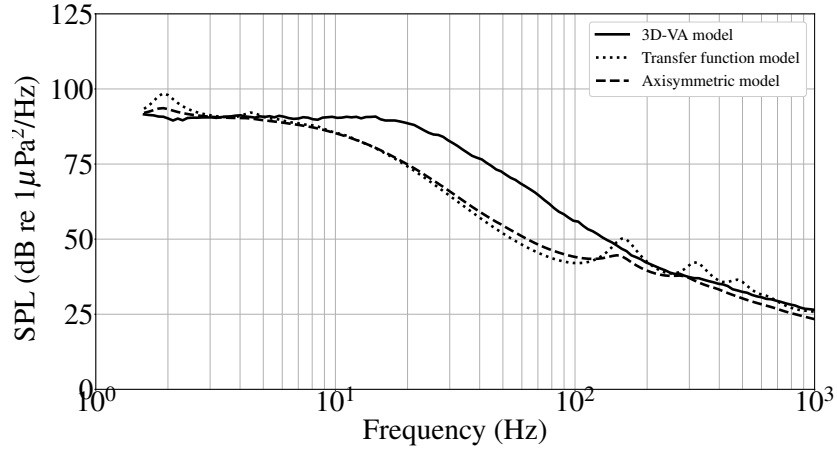


Fig. 11. The on-axis flow noise due to the turbulent pressure excitation computed using the 3D-VA model, the tube transfer function model [9] and the axisymmetric model [11].

4.3 On-axis flow noise for external turbulent pressure excitation

This section presents the flow noise as heard by the hydrophones placed inside the fluid-filled elastic tube. The flow noise is computed using Eqs. (98) and (99). Note that flow noise at a given frequency can be obtained by integrating the corresponding flow noise spectrum (Figs. 9 and 10) over the wavenumber. Fig. 11 shows the variation in flow noise with frequency, computed using the 3D-VA model. It also depicts the flow noise predicted by the tube transfer function [9] and the axisymmetric [11] models. Note that in all cases, the external turbulent pressure excitation is given by Eq. (18) (the hybrid model). The elastic tube, interior fluid and hydrophone parameters are given in Table 1. It can be seen from Fig. 11 that the flow noise decreases with frequency. This decrease is attributed to the reduction in the external turbulent pressure excitation with frequency as shown in Fig. 8. As mentioned earlier, the 3D-VA model considers both $n = 0$ (breathing) and $n = 1$ variation in the acoustic pressure field. This results in a better flow noise prediction than the transfer function and axisymmetric models, where only the $n = 0$ or the breathing wavenumber is considered. The transfer function and the axisymmetric models underpredict the flow noise in the mid frequency range (10 Hz - 200 Hz). It is evident from Figs. 9 and 10 that the difference between the 3D-VA and other models is not significant as the frequency increases. For that reason, the flow noise predictions (Fig. 11) by the three models are quite close to each other at high frequencies (beyond ~ 200 Hz).

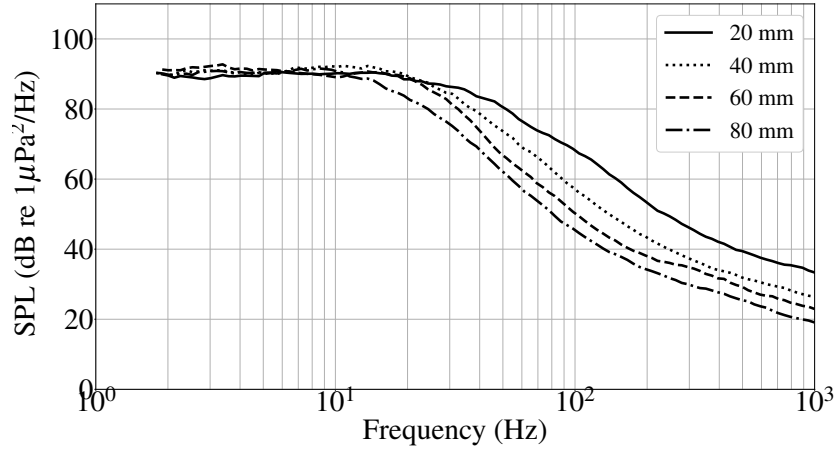


Fig. 12. Comparison of on-axis flow noise estimated using 3D-VA model, due to a turbulent pressure excitation at 5 knots over an elastic tube for different diameters.

4.4 On-axis flow noise for different tube diameters and tow speeds

In this section, the on-axis flow noise (Eqs. (98) and (99)) is computed for different elastic tube diameters at different tow speeds. Fig. 12 shows the comparison of on-axis flow noise estimated for different elastic tube diameters at 5 knots and Fig. 13 shows the variation in the flow noise for a tube of 40 mm diameter at different tow speeds. The variation in flow noise is attributed to the changes in external turbulent pressure excitation with tube diameters and tow speeds, as shown in Fig. 4 (the non-dimensional plot). It was shown in Fig. 4 that an increase in diameter or a decrease in tow speed results in a reduction in the non-dimensional power spectral density. This leads to a decrease in on-axis flow noise inside the fluid-filled elastic tube with increasing tube diameter (Fig. 12) or decreasing tow speeds (Fig. 13).

5 CONCLUSIONS

A new semi-empirical (hybrid) model is developed for estimating the wavenumber-frequency spectrum of turbulent pressure for an axial flow past a solid cylinder. The hybrid model is derived using insights from different turbulent pressure semi-empirical models (Chase [4] and Frendi *et al.* [5]) and the experimental results of Unnikrishnan *et al.* [2]. The hybrid model predictions are found to be superior to the existing semi-empirical models and compares reasonably well with available experimental results.

A fully-coupled three-dimensional vibroacoustic model (3D-VA model) is developed for com-

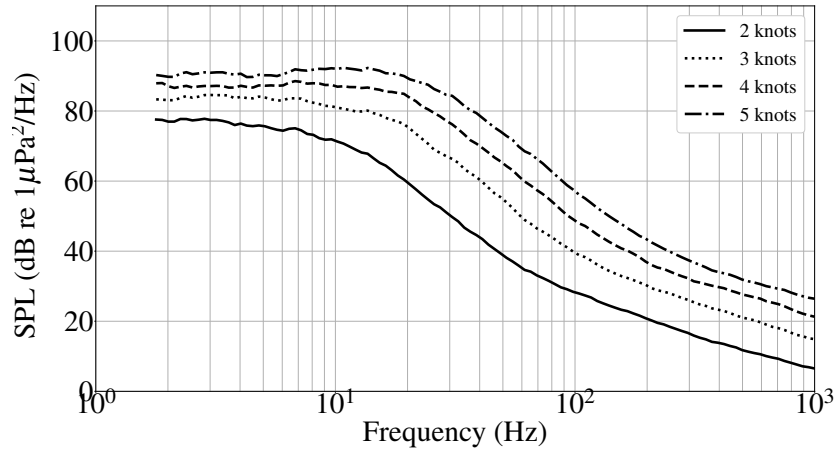


Fig. 13. Comparison of on-axis flow noise estimated using 3D-VA model, due to a turbulent pressure excitation over an elastic tube of 40 mm diameter at different tow speeds.

449 putting the pressure field inside the fluid-filled elastic tube due to external turbulent pressure ex-
 450 citations. In this 3D-VA model, the structure (elastic tube) is modeled using the Navier-Lame
 451 equilibrium equations, and the fluid inside the tube is modeled using the acoustic wave equation.
 452 The 3D-VA model is first tested for an exterior harmonic pressure excitation having a known az-
 453 imuthal variation. The interior pressure field is found to follow the same azimuthal variation as that
 454 of the external excitation.

455 Next, the 3D-VA model is used in conjunction with the hybrid model of the turbulent pressure
 456 spectrum to find the on-axis flow noise. The results are then compared with the on-axis flow noise
 457 estimated using an existing transfer function model [9] and an axisymmetric vibroacoustic model.
 458 The transfer function and the axisymmetric models consider only the breathing mode ($n = 0$) of
 459 the elastic tube, but the 3D-VA model considers both $n = 0$ (breathing) and $n = 1$ (first order)
 460 variations in modeling the elastic tube and the fluid inside the tube. Consequently, it is observed
 461 that the two other models underpredict the flow noise compared to the 3D-VA model.

462 The on-axis flow noise is then estimated for different elastic tube diameters and tow speeds.
 463 At low frequencies, an increase in the tube diameter causes negligible variation in flow noise, but
 464 at higher frequencies, the flow noise decreases with increase in the tube diameter. When the tow
 465 speed is increased, the flow noise is found to increase at all frequencies.

ACKNOWLEDGEMENTS

466 This research was supported by the Defence Research and Development Organisation, India.
467 The authors express their sincere gratitude to Dr. Ganesh Natarajan and Dr. Pramod Kuntikana
468 (Indian Institute of Technology Palakkad) for their invaluable support and guidance throughout
469 this investigation. Special thanks also go to Dr. T. Santhanakrishnan, Mr. Sameer Abdul Azeez,
470 Mr. Jineesh George, Mr. Samuel Theophilus, and Mr. Anshath Hussain (Naval Physical & Oceano-
471 graphic Laboratory) for their invaluable feedback and assistance with this project. We express our
472 gratitude to Prof. A. Seshadri Sekhar, Director of the Indian Institute of Technology Palakkad and
473 Dr. Duvvuri Seshagiri, OS and Director of the Naval Physical & Oceanographic Laboratory, for
474 their support in enabling this collaborative research.

REFERENCES

- [1] Gopi, S., Felix, V. P., Sebastian, S., Pallayil, V., and Kuselan, S., 2010, "In-situ non-acoustic noise measurement system for towed hydrophone array," In 2010 IEEE Instrumentation & Measurement Technology Conference Proceedings, pp. 913–916.
- [2] Unnikrishnan, K. C., Pallayil, V., Chitre, M. A., and Kuselan, S., 2011, "Estimated flow noise levels due to a thin line digital towed array," In OCEANS 2011 IEEE - Spain, pp. 1–4.
- [3] Corcos, G. M., 1963, "Resolution of Pressure in Turbulence," *The Journal of the Acoustical Society of America*, **35**(2), 02, pp. 192–199.
- [4] Chase, D., 1981, "Further modeling of turbulent wall pressure on a cylinder and its scaling with diameter," *NASA STI/Recon Technical Report N*, **82**, p. 29561.
- [5] Frendi, A., and Zhang, M., 2020, "A New Turbulent Wall-Pressure Fluctuation Model for Fluid–Structure Interaction," *Journal of Vibration and Acoustics*, **142**(2), 01, p. 021018.
- [6] Goody, M., 2004, "Empirical spectral model of surface pressure fluctuations," *AIAA Journal*, **42**(9), pp. 1788–1794.
- [7] Francis, R., Ebenezer, D. D., Bhattacharyya, S. K., and Sharma, R., 2023, "Estimation of wavenumber–frequency spectra of wall pressure due to turbulent flow over a flat plate using large-eddy simulation," *Physics of Fluids*, **35**(6), 06, p. 065110.

- [8] Carpenter, A., and Kewley, D., 1983, "Investigation of low wavenumber turbulent boundary layer pressure fluctuations on long flexible cylinders," In Eighth Australasian Fluid Mechanics Conference, Vol. 28, 9A.
- [9] Knight, A., 1996, "Flow noise calculations for extended hydrophones in fluid- and solid-filled towed arrays," *The Journal of the Acoustical Society of America*, **100**(1), 07, pp. 245–251.
- [10] Karthik, K., Jeyakumar, S., and Sebastin, J. S., 2021, "Numerical prediction of flow noise levels on towed sonar array," *Proceedings of the Institution of Mechanical Engineers, Part M: Journal of Engineering for the Maritime Environment*, **235**(2), pp. 600–606.
- [11] Jineesh, G., and Ebenezer, D. D., 2013, "Response of a linear array of hydrophones to flow-induced noise," In Acoustics, New Delhi - India, pp. 1–6.
- [12] Kuttan Chandrika, U., Pallayil, V., Lim, K. M., and Chew, C. H., 2014, "Flow noise response of a diaphragm based fibre laser hydrophone array," *Ocean Engineering*, **91**, pp. 235–242.
- [13] Huang, C., Li, H., and Li, N., 2020, "Flow noise spectrum analysis for vertical line array during descent in deep water," *Journal of Theoretical and Computational Acoustics*, **28**(04), p. 2050022.
- [14] Jordan, S. A., 2014, "On the Axisymmetric Turbulent Boundary Layer Growth Along Long Thin Circular Cylinders," *Journal of Fluids Engineering*, **136**(5), 03, p. 051202.
- [15] Sadd, M., 2014, *Elasticity: Theory, applications, and numerics, third edition* 01.
- [16] Sekharipuram Sekar, R., Natarajan, G., Kuntikana, P., and Akkoorath Mana, A., 2024, "An axisymmetric model for predicting turbulent flow noise in towed sonar arrays," In Proceedings of the 30th International Congress on Sound and Vibration, pp. 1–8.

LIST OF FIGURES

1	Comparison of flow noise predicted by Chase [4] and Frendi [5] models with the experimental results [2] at different tow speeds.	8
2	A comparison of flow noise predicted by the hybrid model, the Chase model [4] and Frendi model [5] with that measured from experiments [2] at different tow speeds. . .	11
3	A comparison of the turbulent pressure spectrum $\hat{p}_0(k_z, \omega)$ given by the hybrid model (Eq. (18)), Chase (Eq. (1)) and Frendi (Eq. (9)) model at 2 knots.	12
4	Non-dimensional power spectral density for different tow speeds using the new hybrid model.	13
5	Fluid filled elastic tube.	14
6	(a): Azimuthal variation in the exterior pressure field $\hat{p}_0(\theta, k_z) = \sin(\theta)$. (b), (c) and (d): Azimuthal variation in the interior pressure field ($r = a$) at 10 Hz, 100 Hz and 1000 Hz, respectively, for $\hat{p}_0(\theta, k_z) = \sin(\theta)$	32
7	(a): Azimuthal variation in the exterior pressure field $\hat{p}_0(\theta, k_z) = \cos(\theta)$. (b), (c) and (d): Azimuthal variation in the interior pressure field ($r = a$) at 10 Hz, 100 Hz and 1000 Hz, respectively, for $\hat{p}_0(\theta, k_z) = \cos(\theta)$	33
8	The external turbulent pressure spectrum level computed using the hybrid model (Eq. (18)).	33
9	Comparison of on-axis flow noise spectrum level due to a turbulent pressure excitation computed using the 3D-VA model and the tube transfer function model [9]. . .	34
10	Comparison of on-axis flow noise spectrum level due to a turbulent pressure excitation computed using the 3D-VA model and the axisymmetric model [11].	35
11	The on-axis flow noise due to the turbulent pressure excitation computed using the 3D-VA model, the tube transfer function model [9] and the axisymmetric model [11].	36
12	Comparison of on-axis flow noise estimated using 3D-VA model, due to a turbulent pressure excitation at 5 knots over an elastic tube for different diameters.	37
13	Comparison of on-axis flow noise estimated using 3D-VA model, due to a turbulent pressure excitation over an elastic tube of 40 mm diameter at different tow speeds. .	38

LIST OF TABLES

1	The elastic tube, interior fluid and the hydrophone array parameters used for estimation of flow noise inside the cylinder	34
---	--	----